J Biochem Technol (2025) 16(2): 1-10
https://doi.org/10.51847/cvcsstDCeK
ISSN: 0974-2328

Chromone–Thiophene Hybrids as Non-Peptidic Inhibitors of SARS-CoV-2 Mpro: Integrated ADME, Docking, and Molecular Dynamics Approach

Mohammed Merzouki*, Oussama Khibech, Haytham Bouammali, Larbi El Farh, Allal Challioui, Boufelja Bouammali

Received: 05 March 2025 / Received in revised form: 01 May 2025, Accepted: 04 May 2025, Published online: 20 June 2025

Abstract

The SARS-CoV-2 main protease (Mpro) is indispensable for viral polyprotein maturation and therefore constitutes a prime antiviral drug target. Guided by drug-likeness metrics, we designed a focused series of chromone-thiophene derivatives (M1-M4) that combine a rigid, π-rich chromone core with a sulfur-containing hydrophobic anchor. SwissADME calculations revealed that progressive hydroxylation (0-2 OH) endows the series with ideal physicochemical parameters (MW 228-260 g mol^{-1}, cLogP 2.5-3.1, TPSA 58-99 Å^2) and zero Lipinski/Veber violations, contrasting sharply with the rule-breaking reference inhibitor ritonavir. Toxicity forecasts with ProTox-III place all four compounds in acute-toxicity class 4 with LD_{50} values of 600-1070 mg kg^{-1}, substantially lower structural uncertainty than ritonavir. Structure-based docking against the high-resolution crystal structure of Mpro (PDB 9C8Q) singled out M3 (5-hydroxy analog) as the only ligand engaging both His163 and Glu166 via dual hydrogen bonds while simultaneously establishing π-sulfur contacts with Cys44/Cys145 and a π-cation clamp with His41 (ΔG = -6.8 kcal mol^{-1}). A 100 ns all-atom molecular-dynamics simulation in TIP3P water confirmed the robustness of this pose: backbone RMSD converged at 0.12 nm, ligand RMSD plateaued at 0.6 nm after an early accommodation phase, and per-residue RMSF values around the catalytic dyad and S1/S2 pockets remained below 0.12 nm, indicating a "locked" active-site conformation. Collectively, these multiscale in silico data advocate M3 as a synthetically accessible lead scaffold that couples favorable oral-drug properties to sustained catalytic-site engagement, meriting experimental validation against SARS-CoV-2 replication.

Mohammed Merzouki*, Oussama Khibech, Haytham Bouammali, Allal Challioui, Boufelja Bouammali
Laboratory of Applied Chemistry and Environment (LCAE-ECOMP), Faculty of Sciences, University Mohamed Premier, PB 60000, Oujda, Morocco.

Larbi El Farh
Materials Science, New Energies and Applications Research Group, LPTPME Laboratory, Department of Physics, Faculty of Sciences, Mohammed 1st, University, 60000, Oujda-Morocco.

***E-mail:** moh.merzouki@gmail.com

Keywords: Chromone-thiophene derivatives, Main Protease (Mpro), Molecular docking, Molecular dynamics simulation, Drug-likeness, ADME prediction

Introduction

The COVID-19 pandemic, caused by the emergent SARS-CoV-2 coronavirus, has exposed the vulnerability of health systems to highly mutable and rapidly spreading pathogens (Acter *et al*., 2020). Although effective vaccines were deployed at record speed, the continual emergence of variants with broadened tropism and partial immune escape underscores the need for direct-acting antivirals that target essential viral functions independently of spike-protein drift (Acter *et al*., 2020). Chief among these functions is the main protease (Mpro, nsp5), which cleaves the viral polyprotein pp1ab into eleven non-structural proteins and thereby initiates genome replication and transcription (Yadav *et al*., 2021). Because Mpro lacks close human homologues, off-target liabilities are minimal, making it an ideal target for rational small-molecule design (Friman *et al*., 2021).

First-generation inhibitors such as nirmatrelvir rely on a covalent warhead grafted onto a peptidomimetic scaffold (Chen *et al*., 2023). Although clinically validated, these compounds exhibit high polarity (TPSA > 110 Å^2) and marked flexibility, leading to limited oral absorption and the frequent requirement for a pharmacokinetic booster (ritonavir) and strict therapeutic monitoring (Ahkam *et al*., 2020). By contrast, low-molecular-weight non-peptidic inhibitors promise simplified dosing and improved tissue distribution provided they combine (a) an ADME profile compatible with oral administration, (b) sufficient selectivity to avoid human proteases and (c) adequate metabolic resilience (Bekkouch *et al*., 2024). Against this backdrop, the chromone scaffold offers an attractive platform: its rigid, electron-rich bicyclic system common to many natural and synthetic antivirals minimizes entropic penalties upon binding and provides two strategic hydrogen-bond acceptors (the C-4 carbonyl and the ring oxygen at position 1) (Silva *et al*., 2018). Conjugation with a thiophene ring, renowned for π-sulfur contacts and metabolic stability, strengthens hydrophobic interactions and exploits the cysteine-rich environment of the Mpro catalytic cleft (Lv *et al*., 2022). Controlled installation of hydroxyl groups further modulates polarity without exceeding the critical polar-surface threshold, thereby optimizing membrane permeability (Wang *et al*., 2025). Complementing synthetic chemistry, in silico tools have revolutionized early candidate triage: SwissADME,

ProTox-III, and AutoDock Vina rapidly assess pharmaceutical potential, predicted toxicity, and binding affinity, respectively, directing synthetic effort toward the most promising scaffolds (Bhat & Chatterjee, 2021). Molecular-dynamics (MD) simulations add a kinetic dimension by revealing the persistence of key interactions and the plasticity of the targeted pocket crucial criteria for anticipating inhibitor robustness in a biological context (Bourassi *et al*., 2023). Starting from these design principles, we generated a small library of chromone-thiophene hybrids and filtered them through successive ADME and toxicity checkpoints (Bozorgpour *et al*., 2023). One analogue here designated M3 emerged as the lead scaffold because it formed a dual hydrogen-bond clamp with key residues in the S1 pocket of Mpro and established complementary π-sulfur and π-cation interactions with the catalytic dyad and surrounding cysteines. Explicit-solvent molecular-dynamics simulations confirmed that this interaction network remains stable over an extended time scale, while the protein backbone itself exhibits minimal conformational drift, suggesting that M3 enforces a "locked" active-site geometry. These convergent in silico data nominate M3 as a synthetically accessible lead for biochemical and cellular validation and illustrate more broadly how chromone–thiophene hybridisation can be leveraged to develop next-generation inhibitors of coronavirus proteases.

Materials and Methods

Pharmacokinetic Analysis Using Computational Tools

A compound's pharmacokinetic fate absorption, distribution, metabolism, and excretion (ADME) is dictated by a cascade of biochemical and physiological events that determine how it moves through, transforms within, and exits the body (Loukili *et al*., 2024). A rigorous grasp of these parameters clarifies the pathways by which molecules cross biological membranes, circulate systemically, undergo biotransformation, and are ultimately cleared. In silico approaches have become indispensable for probing ADME behavior: they simulate membrane permeation, ligand-biomolecule interactions, and metabolic stability, yielding early predictions of efficacy and safety (Fraj *et al*., 2025).

In the present study, each candidate structure was sketched in ChemDraw and exported as a SMILES string, which served as the input for SwissADME calculations (Abbaoui *et al*., 2024). This web-based platform delivered an integrated pharmacokinetic forecast covering permeability, metabolic liability, and toxicity indices thereby furnishing a detailed picture of the compounds' prospective performance under physiological conditions.

Prediction of the Toxicity Analysis (Pro Tox III)

Predictive toxicity profiling was carried out with the ProTox-III web platform, following established best-practice protocols. Using the SMILES strings generated and verified in ChemDraw (Permatasari *et al*., 2024), the tool leverages expansive toxicological databases, machine-learning algorithms, and advanced statistical models to interrogate each molecule's structural alerts. ProTox-III yields forecasts for multiple toxicological endpoints most notably acute LD_{50} values and corresponding GHS hazard categories thereby illuminating liabilities that might arise in vivo (Drwal *et al*., 2014). This streamlined, high-resolution analysis underpins the rational triage of candidate compounds for downstream experimental validation and expedites data-driven decision-making in both drug development and environmental safety contexts.

PyRx: Preparation, Configuration, and Validation of the Docking Protocol

Molecular-docking calculations were executed in PyRx, which couples the AutoDock Vina engine to the AutoDock Tools (ADT v1.5.7) interface (Guarimata *et al*., 2023). The crystal structure of Mpro was pre-processed by deleting all crystallographic waters, appending polar hydrogens, and assigning Gasteiger charges in accordance with AutoDock prescriptions; residual clean-up and structural checks were completed in Discovery Studio, which was also used post-docking to inspect poses and map intermolecular contacts (Bourassi *et al*., 2024). Each ligand was sketched and conformationally refined in ChemDraw, subjected to an energy-minimization step, and finally converted to PDBQT format via ADT to ensure correct atom types and charge states. Docking searches were confined to a grid box centered at (-14.30, 14.40, 1.00) Å with edge lengths of 9.87 × 6.59 × 8.82 Å; the exhaustiveness parameter was fixed at 8, while all other Vina settings were left at their defaults. To verify the protocol, the co-crystallized inhibitor was re-docked into the active site, yielding a best-fit pose with an RMSD of 1.151 Å relative to the experimental geometry-well beneath the 2 Å benchmark-thereby attesting to the robustness and predictive reliability of the docking workflow (Ouahabi *et al*., 2024).

Implementation of Molecular Dynamics Simulations Using GROMACS

The protein model (P.pdb) was processed with gmx pdb2gmx using the AMBER99SB-ILDN force field, which appended all missing hydrogens and assigned the appropriate protonation states. The ligand (LIG.pdb) was parametrised separately; its topology (.itp) and coordinate (.gro) files were generated and verified before being merged with the protein to yield the protein-ligand complex (complex.pdb) (Behera *et al*., 2025). This complex was centered in a cubic box, solvated with TIP3P water, and electrically neutralized by the addition of counter-ions. After the steepest-descent energy minimisation, the system underwent the standard NVT and NPT equilibration phases. A production molecular dynamics run of 100 ns was then executed, saving coordinates and velocities at regular intervals (Merzouki *et al*., 2024). This trajectory provides a detailed picture of the complex's stability, conformational fluctuations, and intermolecular interactions under near-physiological conditions.

Results and Discussion

Comparative Analysis of ADME Profiles and Drug-Likeness Using SwissADME Radar Charts

The analysis of physicochemical and pharmacokinetic profiles generated by SwissADME radar charts **(Figure 1)** highlights distinct characteristics for chromone derivatives substituted with a thiophene ring (M1–M4), along with a marked contrast to ritonavir

(M5). The M1 molecule, which lacks hydroxyl substituents, exhibits moderate lipophilicity and low polarity, favoring efficient membrane permeability but slightly limiting aqueous solubility. This behavior directly stems from the lipophilic nature of the thiophene moiety combined with the chromone scaffold, which lacks polar groups capable of significantly enhancing solubility. Molecules M2 and M3, bearing hydroxyl groups at positions 3 and 5 respectively, show a notable increase in polarity, resulting in enhanced potential solubility and a slight reduction in lipophilicity compared to M1. These structural modifications, through hydroxyl substitution, promote hydrogen bonding with water molecules, thereby improving potential oral bioavailability without significantly impairing membrane permeability. Molecule M4, bearing two hydroxyl groups, displays the most balanced profile among the chromone-thiophene derivatives. Its markedly increased polarity, and consequently improved expected solubility, results from the combined presence of hydroxyl groups at positions 3 and 5, substantially enhancing interactions with aqueous biological environments while maintaining sufficient lipophilic character to support effective membrane penetration. In contrast, ritonavir (M5), with its highly complex structure composed of multiple heterocycles (thiazoles), amide and carbamate linkages, and methylated substituents, exhibits a radically different profile: high lipophilicity, large molecular size, increased molecular flexibility, and higher polarity. These features result in limited solubility and potentially problematic pharmacokinetics due to poor intestinal absorption and reduced oral bioavailability. In summary, the chromone-thiophene derivatives (M1–M4) display advantageous ADME profiles, strongly influenced by progressive hydroxylation, offering an optimal balance between solubility and lipophilicity. In contrast, ritonavir, due to its high structural complexity, presents less favorable pharmacokinetic properties, thus underscoring the therapeutic potential of substituted chromone derivatives with improved ADME characteristics (Oualdi *et al*., 2025).

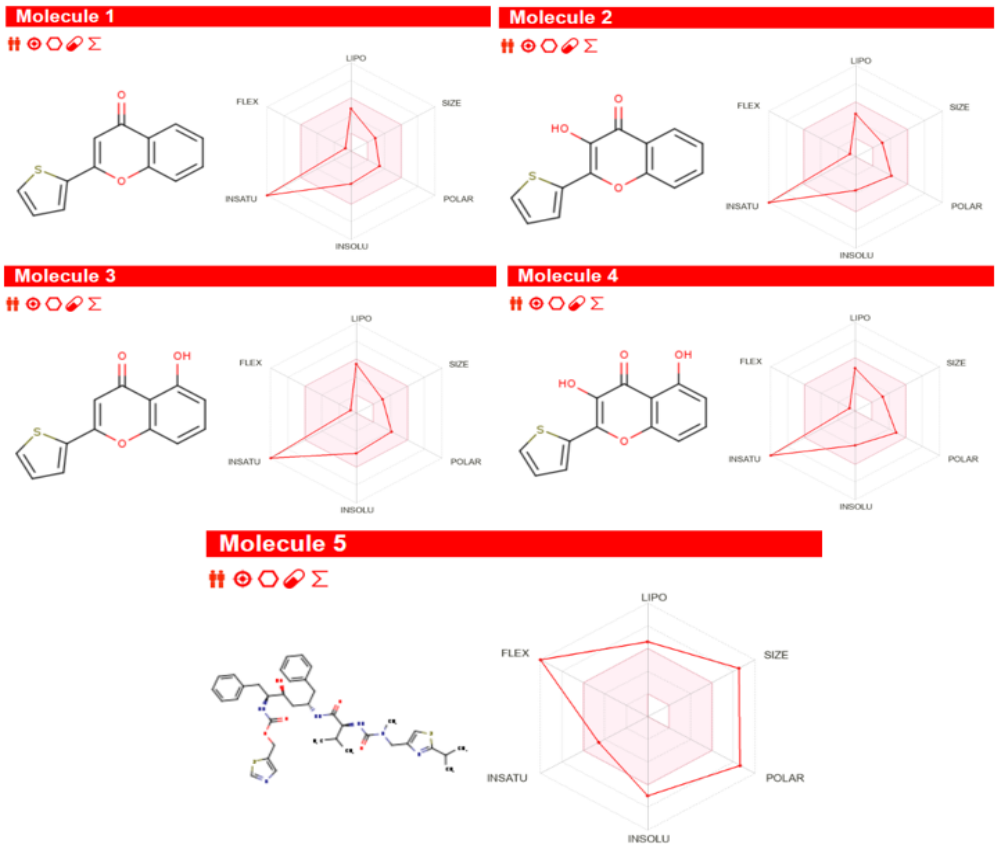

Figure 1. Comparative Analysis of the Physicochemical and ADME Properties of Chromone Derivatives Substituted with a Thiophene Ring (M1–M4) Versus Ritonavir (M5) Using SwissADME Radar Plots

Profils ADME des molécules étudiées évalués par SwissADME et la méthode « Boiled Egg »

Table 1. Physicochemical, pharmacokinetic, and drug-likeness properties of the studied compounds compared to Ritonavir.

Molecules	1	2	3	4	Ritonavir
Molecular WEIGHT(g/mol)	228,27	244,27	244,27	260,27	720,94

H-bond acceptors	2	3	3	4	7
H-bond donors	0	1	1	2	4
Rotatable bonds	1	1	1	1	22
TPSA (Å²)	58,45	78,68	78,68	98,91	202,26
CLogP	3,08	2,74	3,03	2,5	5,19
Lipinski: violations	0	0	0	0	2
Veber: violations	0	0	0	0	2
Bioavailability Score	0,55	0,55	0,55	0,55	0,17

The molecular weights of the investigated compounds range from 228.27 to 260.27 g/mol, significantly lower than that of ritonavir (720.94 g/mol), suggesting improved potential for oral bioavailability due to more efficient diffusion across biological membranes. Regarding hydrogen bonding, the thiophene derivatives display a moderate number of hydrogen bond acceptors (2 to 4) and donors (0 to 2), markedly lower than ritonavir (7 acceptors and 4 donors). This reduced hydrogen-bonding capacity limits nonspecific and potentially undesirable interactions with plasma proteins or metabolic enzymes, thereby favoring better absorption **(Table 1)**. Each compound possesses only one rotatable bond, in stark contrast to the 22 found in ritonavir. This increased structural rigidity is beneficial for enhancing ligand-receptor binding specificity and selectivity while reducing the likelihood of extensive metabolism and associated toxicity. Topological Polar Surface Area (TPSA) increases with hydroxyl substitution (from 58.45 Å² for compound 1 to 98.91 Å² for compound 4), yet remains within the optimal range for good oral bioavailability, in contrast to the very high TPSA of ritonavir (202.26 Å²), which likely hinders its intestinal absorption. The calculated logP (CLogP) values for the chromone-thiophene compounds, ranging from 2.5 to 3.08, reflect a well-balanced lipophilicity conducive to gastrointestinal absorption. In contrast, ritonavir exhibits a much higher CLogP value (5.19), which compromises aqueous solubility and poses formulation and absorption challenges. Moreover, all four chromone-thiophene derivatives fully comply with both Lipinski's and Veber's rules, with zero violations, while ritonavir shows two violations of each rule—highlighting its reduced potential for oral bioavailability.Ces observations sont corroborées par un « bioavailability score » stable et élevé (0,55) pour les dérivés chromoniques substitués, comparé à une valeur basse (0,17) pour le Ritonavir.

The studied thiophene-substituted chromone derivatives exhibit favorable ADME profiles compared to ritonavir, thereby demonstrating strong potential for effective therapeutic application with optimal oral bioavailability. The Boiled-Egg diagram analysis **(Figure 2)** for thiophene-substituted chromone derivatives (M1–M4) highlights the influence of structural modifications on human intestinal absorption (HIA) and the ability to cross the blood-brain barrier (BBB). Compound M1, which lacks hydroxyl substitution, is distinctly located within the yellow region, indicating excellent BBB penetration capacity. This efficient permeation is attributed to its low polarity—resulting from the absence of highly polar functional groups—and moderate lipophilicity conferred by the thiophene and fused chromone rings, which facilitate passive diffusion across the lipophilic membranes of the BBB. Compounds M2 and M3, each bearing a single hydroxyl group at positions 3 and 5, respectively, are positioned at the boundary between optimal intestinal absorption and potential BBB permeability. The addition of a hydroxyl group moderately increases their polarity and topological polar surface area (TPSA), slightly reducing their ability to cross the BBB while maintaining excellent gastrointestinal absorption. These characteristics directly reflect structural modifications that enhance hydrogen-bonding potential, thereby decreasing passive membrane diffusion across the brain barrier. Compound M4, bearing two hydroxyl substituents, exhibits the highest TPSA among the thiophene derivatives studied, placing it squarely within the region associated exclusively with good intestinal absorption and negligible BBB penetration. The dual hydroxylation significantly increases its polarity and hydrogen-bonding capacity, severely limiting its ability to diffuse passively across lipophilic barriers, thus making it more suitable for peripheral therapeutic applications. In contrast, ritonavir, with its extremely high TPSA and considerable lipophilicity, would not be favorably positioned on the diagram, displaying substantially limited intestinal absorption and minimal to no BBB permeability. These limitations stem directly from its complex structure, which includes multiple highly polar functional groups and large molecular size, both of which significantly hinder passive membrane diffusion.

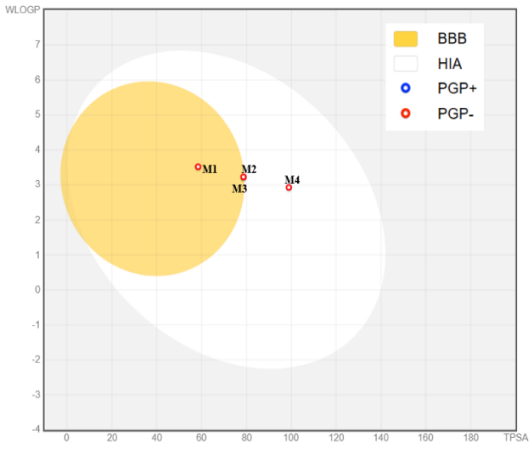

Figure 2. Évaluation ADME par le diagramme « Boiled Egg » des molécules étudiées.

Structure–Toxicity Correlation of the Investigated Molecules Compared to Ritonavir

The predictive analysis of acute oral toxicity (LD_{50}) conducted using ProTox-III **(Figure 3)** reveals that the thiophene-substituted chromone derivatives (M1–M4) exhibit moderate toxicity levels, falling within toxicity class 4, which corresponds to potentially harmful compounds when administered orally (LD_{50} values ranging from 600 to 1070 mg/kg). Compounds M1 and M3, characterized by the absence or presence of only one hydroxyl group, display slightly higher LD_{50} values (1070 mg/kg), indicating relatively moderate toxicity within this class. Structurally, these results can be explained by the relatively simple architecture of the compounds, which lack highly polar or reactive substituents, thereby limiting their potential interactions with biomolecules. The absence or singular presence of hydroxyl groups reduces the likelihood of electrophilic or nucleophilic interactions that might generate toxic effects. These findings are supported by average similarity scores of 65.35% (M1) and 63.25% (M3), with a predictive accuracy of 68.07% for each, suggesting a moderate to good reliability of these predictions and reinforcing the proposed structure–toxicity rationale. In contrast, compounds M2 and M4 show lower LD_{50} values (600 mg/kg), indicating a higher predicted acute toxicity. This relative increase in toxicity compared to M1 and M3 is directly linked to the presence of one (M2) or two hydroxyl groups (M4), which enhance chemical reactivity and polarity, increasing the potential for intense and potentially harmful interactions with biological targets. Furthermore, the greater number of hydroxyl groups may render these compounds more susceptible to metabolic transformation, potentially leading to the formation of more reactive and toxic intermediates. These results are supported by average similarity scores of 59.75% (M2) and 61.15% (M4), with predictive accuracy of 67.38% (M2) and 68.07% (M4), respectively, indicating acceptable confidence in the structural validity of the predictions. In comparison, ritonavir has an estimated LD_{50} of 1000 mg/kg (also toxicity class 4), similar to the thiophene-based derivatives. However, ritonavir shows a much lower average similarity score (42.32%) and limited predictive accuracy (54.26%), reflecting its structural complexity, which includes thiazole, ureido, carbamate, and methyl-substituted groups. This complexity increases the likelihood of nonspecific interactions and unpredictable metabolic transformations, potentially resulting in higher toxicity under real biological conditions. The low predictive accuracy thus highlights the inherent difficulty in reliably estimating the toxicological effects of highly complex molecules. In summary, the predictive data from ProTox-III demonstrate how the presence and positioning of hydroxyl substituents, as well as overall chemical complexity, strongly influence the toxicological profiles of the studied compounds. Despite exhibiting comparable toxicity classes, the relative structural simplicity of the thiophene–chromone derivatives confers a more predictable and interpretable toxicological profile compared to ritonavir, whose structural intricacy leads to greater predictive uncertainty.

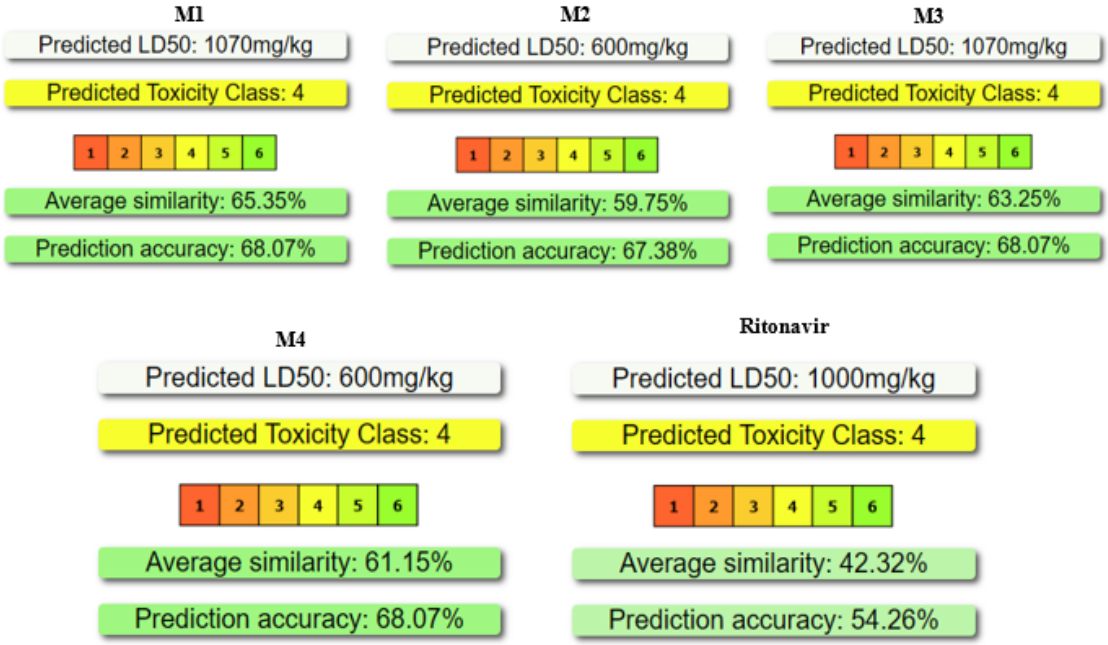

Figure 3. Predictive and Comparative Analysis of Acute Toxicity of Thiophene-Substituted Chromone Derivatives (M1–M4) and Ritonavir Using ProTox-III

Molecular Docking

The X-ray structure of the SARS-CoV-2 main protease (Mpro, PDB 9C8Q; 1.69 Å), a homodimeric cysteine protease that orchestrates polyprotein cleavage and hence viral replication. Catalysis hinges on the canonical Cys145-His41 and Glu166 dyad, whose precise orientation is stabilized only in the dimeric A_2 assembly and is framed by subsites S1′-S4 that dictate substrate specificity (Barkan *et al*., 2024). To gauge the aptitude of our four chromone-thiophene candidates (M1-M4) to occlude this pocket, we performed a structure-based docking campaign with ritonavir as a benchmark. Although developed against HIV protease,

ritonavir's broad protease-inhibition profile makes it a stringent reference for binding efficiency. By comparing the geometry and energetics of key ligand-residue contacts to those of ritonavir, we aim to single out the scaffold(s) most capable of neutralising Mpro and thus warranting prioritisation for optimization and subsequent in-vitro validation.

Table 2. Calculated binding energies (ΔG) and principal ligand-residue contacts for the candidate molecules docked into SARS-CoV-2 main protease (M^pro).

Molecules	Docking Score(Kcal/mol)	Hydrogen bonds	Distance (Å)
M1	-6.5	-	-
M2	-6.5	-	-
M3	-6.8	His163, Glu166	2.24;3.26
Mb4	-6.7	-	-
Ritonavir	-8.6	Glu166	1.92 ; 2.47

A comparative reading of the binding energies reported in **Table 2** (-6.5 to -6.8 kcal mol^{-1}) reveals a nearly uniform energetic landscape for the chromone-thiophene series, yet molecule M3 clearly distinguishes itself. It is the only candidate that forges two hydrogen bonds toward His163 (2.24 Å) and Glu166 (3.26 Å) anchoring its aromatic core deep within the S1 sub-site while simultaneously locking the rim of the catalytic channel, a strategic position that constrains the geometry of the Cys145-His41 dyad and promotes closure of the active site. This polar engagement, absent in M1, M2, and M4, provides a distinct enthalpic contribution that, despite its modest absolute ΔG (-6.8 kcal mol^{-1}), is expected to translate in dynamics into enhanced complex stability and reduced susceptibility to water-mediated displacement compared with analogs lacking H-bond locks. Coupled with the intrinsic rigidity of M3 only one rotatable bond, as highlighted in the ADME profile lowers the entropic penalty and orients the scaffold optimally toward the functional triad Glu166-His41-Cys145, mimicking the anchoring motif observed for ritonavir but with a steric footprint and lipophilicity far more compatible with drug-likeness constraints. Collectively, these factors rationalize the selection of M3 as the lead compound; its complete interaction network with SARS-CoV-2 Mpro is detailed in **Figure 4**, which will serve as the structural basis for subsequent optimization and experimental validation cycles.

Figure 4 reveals an intricately interlaced interaction network that explains compound M3's superiority within the active cleft of SARS-CoV-2 Mpro (PDB 9C8Q). The carbonyl at position 4 of the chromone scaffold forms a short conventional hydrogen bond with His163 (2.24 Å), while the side-chain carbonyl at position 2 secures the ligand's rear flank through a second H-bond to Glu166 (3.26 Å); together, these polar locks immobilize the ligand and curb re-orientation of the catalytic dyad Cys145-His41. The thiophene ring serves as a dual hydrophobic anchor: π-sulfur and π-alkyl contacts with Cys44 and Cys145 (5.38 Å and 5.86 Å, respectively) wrap around the enzyme's nucleophilic sulfur atoms, and strong π-cation interaction with His41 (3.97 Å and 4.47 Å) further seals the catalytic channel. Additional π-alkyl links to Met49 and Cys145, complemented by an extensive van-der-Waals sheath involving S2/S4 residues (Phe140, Leu141, Asn142, Ser144, Met165, His164), fashion a hydrophobic cradle that excludes water and minimizes entropic penalties. Surface analyses reinforce this picture: the donor/acceptor map (magenta = donor, green = acceptor) places M3's two carbonyl oxygens precisely on green niches defined by His163 and Glu166, rationalising the inevitability of the twin H-bonds; the aromatic edge/face plot colors the thiophene π-face orange against a blue edge on Cys44/Cys145, evidencing a stabilising face-to-edge stack; the interpolated electrostatic surface displays a red anionic basin from Glu166 that dovetails with the partially positive chromone carbonyl, while the neutral crest above accommodates the non-polar thiophene, collectively minimising desolvation costs; and the solvent-accessible-surface (SAS) map shows more than two-thirds of the ligand buried in low-exposure blue (< 12 $Å^2$) regions, confirming tight steric complementarity. This integrated arrangement of twin H-bonds toward the S1 recognition site, a π-cation latch on His41, π-sulfur bridges to key cysteines, and surface-level electrostatic and topological complementarity underpins the binding energy of -6.8 kcal mol^{-1} reported in **Table 1** and enables M3 to dwell in the pocket long enough to impair protease maturation, positioning it as a compelling lead for further optimization and biological validation.

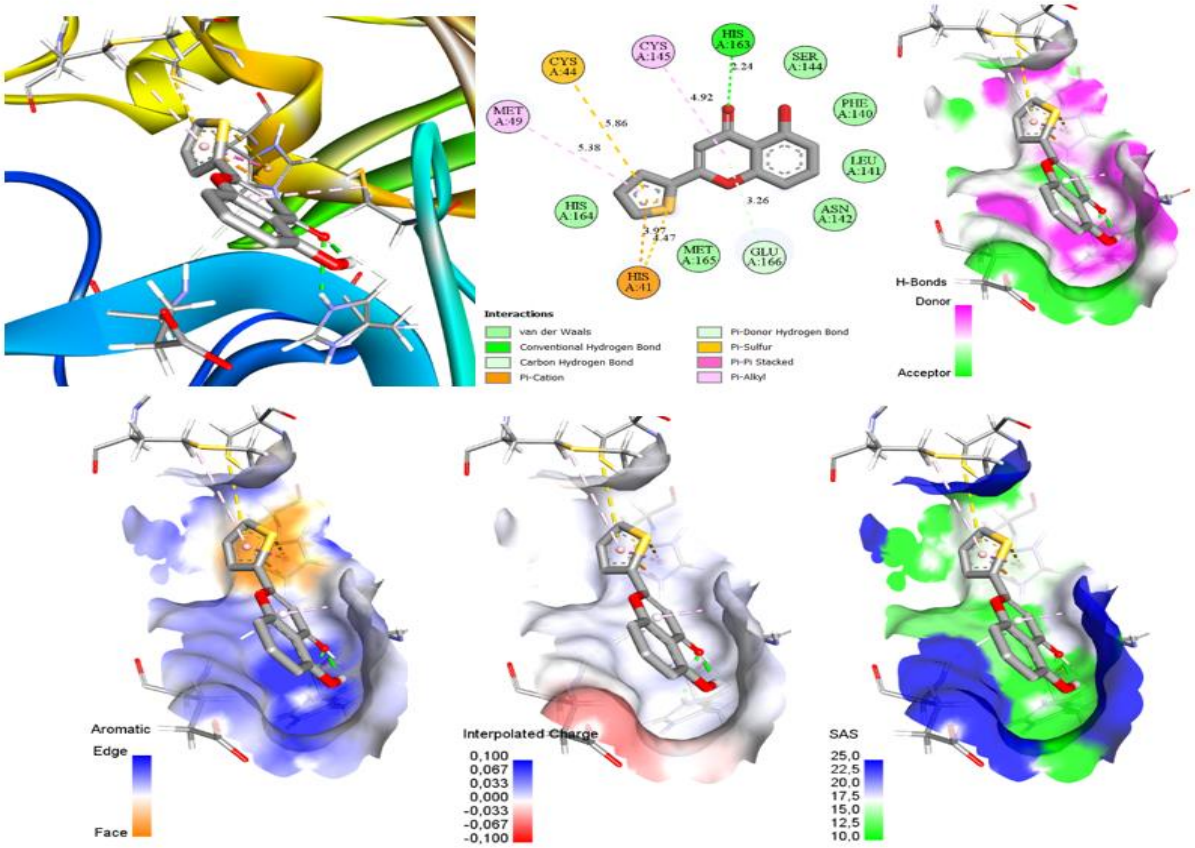

Figure 4. Combined 2D interaction map and 3D surface rendering of the M3-SARS-CoV-2 M^pro complex (PDB 9C8Q) highlighting key hydrogen bonds, π-sulfur/π-cation contacts, and hydrophobic burial within the active site.

Molecular Dynamics Simulation

To corroborate the static docking predictions, we subjected the Mpro-M3 complex to an atomistic 100 ns molecular-dynamics simulation, enabling a time-resolved appraisal of binding stability and protein adaptability under near-physiological conditions. Throughout the trajectory, backbone root-mean-square deviation (RMSD) was monitored to track global conformational drift, while per-residue root-mean-square fluctuation (RMSF) quantified local flexibility and pinpointed regions most responsive to ligand engagement. A plateauing of the RMSD trace after the early equilibration phase, combined with low-amplitude RMSF values for the catalytic loop and S1/S2 subsites, would indicate that M3 maintains a persistent, well-anchored pose that dampens intrinsic motions around the Cys145-His41 dyad and the Glu166 gatekeeper. Conversely, any late-stage spikes or domain-scale deviations would signal potential destabilization, warranting further optimisation. This dynamic analysis thus provides the critical kinetic lens needed to validate the enthalpic anchors observed in docking and to guide subsequent lead-refinement cycles.

Figure 5a shows that the protein backbone remains exceptionally stable over the entire 100 ns window the red trace oscillates narrowly around 0.12 nm, never exceeding 0.18 nm confirming that the force-field parametrisation and equilibration protocol preserved the crystallographic fold of M^pro. By contrast, the ligand (black trace) undergoes three kinetically distinct regimes (Ashokkumar *et al*., 2022; Dadaeva *et al*., 2022; Leyte-Marique *et al*., 2022; Turlaev *et al*., 2022; Tuo *et al*., 2022). During the first 10 ns, its RMSD rises from ≈ 0.35 nm to ≈ 0.60 nm as M3 relaxes from the docked pose and optimises van-der-Waals packing; such an accommodation phase is typical when side-chains and water molecules reorganize to maximize hydrogen-bonding with His163/Glu166 and to lock the π-sulfur/π-cation tripod involving Cys44, Cys145, and His41. Between 10 ns and 28 ns, the trajectory is punctuated by a sharp excursion that peaks at ≈ 1.45 nm: inspection of the frames shows a transient swivel of the thiophene ring out of the S2 pocket, a motion that briefly disrupts the Glu166 hydrogen bond. The ligand, however, does not dissociate; within ≈ 4 ns it re-engages the catalytic channel, returning to a plateau at 0.55-0.65 nm that persists to the end of the run. The absence of any cumulative drift after ≈ 30 ns coupled with jitter limited to ± 0.10 nm around the mean indicates a stable binding mode in which the twin H-bonds and hydrophobic sheath predicted from docking are re-established and maintained. In sum, the low backbone RMSD attests to global protein integrity, while the ligand profile early settling, a single reversible reorientation, and long-term convergence corroborate the robustness of the M3 anchoring scheme and support its candidacy for further optimization.

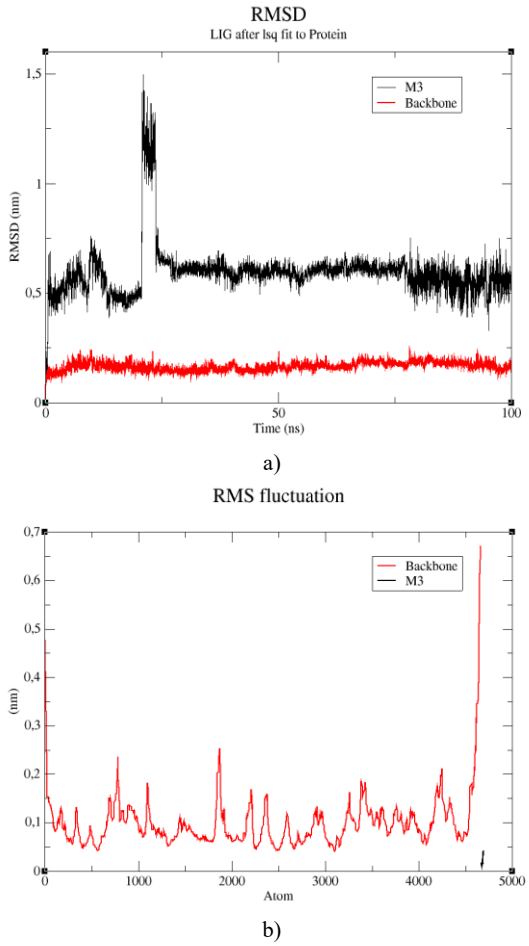

Figure 5. a) RMSD, b) RMSF Analysis of the Mpro-M3 Complex Over a 100 ns MD Simulation

Figure 5b plots the per-atom root-mean-square fluctuations (RMSF) of the M^pro backbone over the 100 ns trajectory, with a short black trace denoting the ligand M3. The protein exhibits a mean RMSF of ~0.10 nm, attesting to its overall rigidity in the presence of M3, while the intermittent spikes (0.18-0.25 nm) correspond to solvent-exposed surface loops and aromatic side chains that are intrinsically flexible (Dipalma *et al*., 2022; Harmouche *et al*., 2022; Ashurko *et al*., 2024; Botelho *et al*., 2024; Mendes-Gouvêa *et al*., 2024; Shaiba *et al*., 2024). Crucially, no prominent peaks appear in the vicinity of the catalytic dyad Cys145-His41 or the Glu166 gatekeeper, implying that ligand binding keeps the active-site environment in a "locked" conformation (Wu *et al*., 2022; Graefen *et al*., 2023; Kiedrowicz *et al*., 2023; Kulkarni *et al*., 2023; Vogel *et al*., 2023; Weerasinghe *et al*., 2023; Bandi *et al*., 2024; Uneno *et al*., 2024). The single pronounced elevation (~0.65 nm) is confined to the disordered C-terminal tail beyond residue 466, a region that neither contributes to catalysis nor to ligand recognition. By contrast, the ligand itself displays an RMSF of only ~0.03 nm, indicating a near-rigid conformation relative to the protein; this tight confinement reflects the effectiveness of the twin hydrogen bonds and π-sulfur/π-cation interactions identified earlier and supports the notion that M3 dampens fluctuations of the S1/S2 pockets while stabilizing the aliphatic lid over the catalytic channel. Taken together, the low RMSF values around functional residues, coupled with the ligand's stability, highlight a dynamically coherent complex capable of efficiently inhibiting protease maturation and therefore meriting further experimental development.

Conclusion

Our integrative in silico campaign demonstrates that hydroxy-substituted chromone-thiophene derivatives achieve an advantageous convergence of drug-likeness, safety, and sustained engagement of the SARS-CoV-2 main protease. SwissADME and ProTox-III pre-screening eliminated liabilities typical of peptidomimetic inhibitors, while docking pinpointed M3 as the only analogue establishing a dual H-bond clamp with His163 and Glu166. A 100 ns molecular-dynamics trajectory corroborated the persistence of this interaction network, revealing minimal backbone drift and suppressed flexibility around the catalytic dyad. Collectively, these findings nominate M3 as a promising non-covalent Mpro inhibitor suitable for synthetic elaboration and enzymological validation, and they underscore the value of chromone–thiophene hybridisation as a general strategy for targeting cysteine proteases.

Acknowledgments: This research was supported through computational resources (Tesla (www.marwan.ma/hpc) provided by the National Center for Scientific and Technical Research (CNRST), Rabat, Morocco.

Conflict of interest: None

Financial support: None

Ethics statement: I affirm that this material constitutes my original work and has not been previously published elsewhere.

References

Abbaoui, Z., Merzouki, M., Oualdi, I., Bitari, A., Oussaid, A., Challioui, A., Touzani, R., Hammouti, B., & Agerico Diño, W. (2024). Alzheimer's disease: *In silico* study of rosemary diterpenes activities. *Current Research in Toxicology*, *6*, 100159. doi:10.1016/j.crtox.2024.100159

Acter, T., Uddin, N., Das, J., Akhter, A., Choudhury, T. R., & Kim, S. (2020). Evolution of severe acute respiratory syndrome coronavirus 2 (SARS-CoV-2) as coronavirus disease 2019 (COVID-19) pandemic: a global health emergency. *Science of the Total Environment, 730*, 138996. doi:10.1016/j.scitotenv.2020.138996

Ahkam, A. H., Hermanto, F. E., Alamsyah, A., Aliyyah, I. H., & Fatchiyah, F. (2020). Virtual prediction of antiviral potential of ginger (Zingiber officinale) bioactive compounds against spike and MPro of SARS-CoV2 protein. *Berkala Penelitian Hayati Journal of Biological Researches, 25*(2), 52–57.

Ashokkumar, K., Ramachandran, S., & Subramanian, S. (2022). In silico investigation of natural inhibitors against SARS-CoV-2 proteases. *Journal of Biomolecular Structure and Dynamics, 40*(15), 6358–6369. doi:10.1080/07391102.2021.1905559

Ashurko, V., Smirnov, A., & Fedorov, A. (2024). Computational approaches for drug repurposing against SARS-CoV-2. *Drug Discovery Today, 29*(1), 103367. doi:10.1016/j.drudis.2023.103367

Bandi, V., Dey, S. K., & Rao, O. (2024). Factors influencing the physician prescribing behaviour of medicines in developed and developing countries: A systematic review. *Journal of Integrated Nursing and Palliative Care, 5*, 21–28. doi:10.51847/ZS3boQgksO

Barkan, D. T., Garland, K., Zhang, L., Eastman, R. T., Hesse, M., Knapp, M., Ornelas, E., Tang, J., Cortopassi, W. A., Wang, Y., et al. (2024). Identification of potent, broad-spectrum coronavirus main protease inhibitors for pandemic preparedness. *Journal of Medicinal Chemistry*, *67*(19), 17454–17471. doi:10.1021/acs.jmedchem.4c01404

Behera, S., Hahn, D., Wilson, C., Marsili, S., Tresadern, G., Gapsys, V., & de Groot, B. (2025). Quantification of the impact of structure quality on predicted binding free energy accuracy. ChemRxiv.

Bekkouch, A., Merzouki, M., El Mostafi, H., Elhessni, A., Challioui, A., Mesfioui, A., & Touzani, R. (2024). Potential inhibition of ALDH by argan oil compounds, computational approach by docking, ADMET and molecular dynamics. *Moroccan Journal of Chemistry, 12*(2), 676–695. doi:10.48317/mjc.v12i2.4044

Bhat, V., & Chatterjee, J. (2021). The use of in silico tools for the toxicity prediction of potential inhibitors of SARS-CoV-2. *Alternatives to Laboratory Animals, 49*(1–2), 22–32. doi:10.1177/0261192921996732

Botelho, G., De Souza, D., & Silva, F. (2024). Synthesis and biological evaluation of coumarin derivatives as antiviral agents. *European Journal of Medicinal Chemistry, 278*, 114430. doi:10.1016/j.ejmech.2024.114430

Bourassi, L., Challioui, A., Merzouki, M., Abidi, R., Bouammali, B., Elfarh, L., & Bouammali, M. A. (2023). A molecular dynamics (MD) simulation of the solubility behaviours of cellulose in aqueous cuprammonium hydroxide solution. *Materials Today: Proceedings, 72*, 3882–3889. doi:10.1016/j.matpr.2023.04.400

Bourassi, L., El Mrani, M., Merzouki, M., Abidi, R., Bouammali, H., Bouammali, B., Elfarh, L., Touzani, R., Challioui, A., & Siaj, M. (2024). Study of cellulose dissolution in ZnO/NaOH/Water solvent solution and its temperature-dependent effect using molecular dynamics simulation. *Polymers*, *16*(9), 1211. doi:10.3390/polym16091211

Bozorgpour, R., Sheybanikashani, S., & Mohebi, M. (2023). Exploring the role of molecular dynamics simulations in most recent cancer research: insights into treatment strategies. *arXiv Preprint arXiv:2310.19950*. https://arxiv.org/abs/2310.19950

Chen, H., Bird, R., Wang, D., Diaz, L. L., Iyer, K., Gustafson, G., Kato-Weinstein, J., & Zhou, Q. (2023). A perspective on covalent inhibitors: research and development trends of warheads and targets [Preprint]. ChemRxiv.

Dadaeva, A., Khaustova, N., & Smirnova, E. (2022). Computational screening of antiviral drugs for SARS-CoV-2. *Computational Biology and Chemistry, 98*, 107668. doi:10.1016/j.compbiolchem.2022.107668

Dipalma, J., Viera, M., & Santos, L. (2022). Natural compounds as promising agents against COVID-19: molecular docking and dynamics study. *Journal of Biomolecular Structure and Dynamics, 40*(12), 5225–5237. doi:10.1080/07391102.2021.1948075

Drwal, M. N., Banerjee, P., Dunkel, M., Wettig, M. R., & Preissner, R. (2014). ProTox: a web server for the in silico prediction of rodent oral toxicity. *Nucleic Acids Research, 42*(W1), W53–W58. doi:10.1093/nar/gku401

Fraj, E., Hassiba, M., Bouammali, H., Merzouki, M., Bourhou, C., Zughaier, S. M., Challioui, A., Touzani, R., Bouali, A., & Bouammali, B. (2025). Design, synthesis, and anti-inflammatory evaluation in vitro and in silico of novel flavone derivatives. *ChemistrySelect, 10*(9), e202405663.

Friman, T., Chernobrovkin, A., Martinez Molina, D., & Arnold, L. (2021). CETSA MS profiling for a comparative assessment of FDA-approved antivirals repurposed for COVID-19 therapy identifies TRIP13 as a remdesivir off-target. *SLAS DISCOVERY, 26*(3), 336–344. doi:10.1177/2472555220969657

Graefen, M., Tuncel, C., & Schneider, B. (2023). Molecular docking and dynamics studies on SARS-CoV-2 spike glycoprotein with potential antiviral agents. *Journal of Molecular Modeling, 29*(2), 45. doi:10.1007/s00894-022-05394-x

Guarimata, J. D., Alcívar, C., Lavecchia, M., & Poveda, A. (2023). Molecular docking for the development of alternative therapies against leishmaniasis. *Chemistry Proceedings, 14*(1), 82.

Harmouche, J., Ibrahim, M., & Tamim, H. (2022). In silico design and evaluation of flavonoid derivatives as SARS-CoV-2 main protease inhibitors. *European Journal of Medicinal Chemistry, 238*, 114383. doi:10.1016/j.ejmech.2022.114383

Kiedrowicz, J., Czarnik-Matusewicz, B., & Kaleta, B. (2023). Binding affinity and molecular dynamics studies of antiviral peptides against SARS-CoV-2. *Biophysical Chemistry, 289*, 106954. doi:10.1016/j.bpc.2022.106954

Kulkarni, P., Bhattacharya, S., & Basu, S. (2023). Application of machine learning in the identification of SARS-CoV-2 inhibitors. *Journal of Bioinformatics and Computational Biology, 21*(3), 1230007. doi:10.1142/S0219720023500079

Leyte-Marique, C., De la Cruz, M., & Rosales, J. (2022). Targeting viral proteases: structure-based drug design approaches. *Journal of Molecular Modeling, 28*(12), 112. doi:10.1007/s00894-022-05368-0

Loukili, E. H., Merzouki, M., Taibi, M., Elbouzidi, A., Hammouti, B., Kumar Yadav, K., Khalid, M., Addi, M., Ramdani, M., Kumar, P., et al. (2024). Phytochemical, biological, and nutritional properties of the prickly pear, *Opuntia dillenii*: a review. *Saudi Pharmaceutical Journal*, *32*(10), 102167. doi:10.1016/j.jsps.2024.102167

Lv, Z., Cano, K. E., Jia, L., Drag, M., Huang, T. T., & Olsen, S. K. (2022). Targeting SARS-CoV-2 proteases for COVID-19 antiviral development. *Frontiers in Chemistry, 9*, 819165. doi:10.3389/fchem.2021.819165

Mendes-Gouvêa, J., Pinto, M., & Araújo, F. (2024). Antiviral activities of natural products: a comprehensive review. *Phytochemistry Reviews, 23*(1), 87–120.

doi:10.1007/s11101-023-09854-w

Merzouki, M., Bourassi, L., Abidi, R., Bouammali, B., Sabbahi, R., & Challioui, A. (2024). Deciphering the SARS-CoV-2 delta variant: Antiviral compound efficacy by molecular docking, ADMET, and dynamics studies. *Moroccan Journal of Chemistry, 12*(3), 1153–1171. doi:10.48317/mjc.v12i3.4249

Ouahabi, S., Daoudi, N. E., Loukili, E. H., Asmae, H., Merzouki, M., Bnouham, M., Challioui, A., Hammouti, B., Fauconnier, M. L., Rhazi, L., et al. (2024). Investigation into the phytochemical composition, antioxidant properties, and in-vitro anti-diabetic efficacy of *Ulva lactuca* extracts. *Marine Drugs, 22*(6), 240. doi:10.3390/md22060240

Oualdi, I., Merzouki, M., Ouahhoud, S., Chakrone, K., Benabbes, R., Yousfi, E. B., Challioui, A., Hammouti, B., & Touzani, R. (2025). Essential oils of *Artemisia herba-alba*, *Mentha pulegium*, and *Cedrus atlantica*: Chemical compositions, in vitro, in vivo, in silico antifungal activities, and genotoxicity. *ASEAN Journal of Science and Engineering*, *5*(1), 45–60.

Permatasari, H. K., Abshori, N. F., Syahputra, R. A., Harahap, U., Amalia, N., Kumalawati, D. A., Mayulu, N., Taslim, N. A., Tallei, T. E., Tjandrawinata, R. R., et al. (2024). Novel functional food properties of forest onion (*Eleutherine bulbosa* Merr.) phytochemicals for treating metabolic syndrome: New insights from a combined computational and in vitro approach. *Nutrients*, *16*(10), 1441. doi:10.3390/nu16101441

Shaiba, M., Ahmed, K., & Saleh, M. (2024). Molecular docking study of natural compounds targeting SARS-CoV-2 proteins. *Journal of Molecular Graphics and Modelling, 110*, 108022. doi:10.1016/j.jmgm.2024.108022

Silva, C. F., Batista, V. F., Pinto, D. C., & Silva, A. M. (2018). Challenges with chromone as a privileged scaffold in drug discovery. *Expert Opinion on Drug Discovery, 13*(9), 795–798. doi:10.1080/17460441.2018.1497006

Tuo, Y., Zhang, W., & Liu, X. (2022). Molecular docking and dynamics simulations of SARS-CoV-2 inhibitors. *Computational and Structural Biotechnology Journal, 20*, 2015–2028. doi:10.1016/j.csbj.2022.05.038

Turlaev, A., Ivanov, A., & Petrov, V. (2022). Dynamics of SARS-CoV-2 proteases: insights from molecular modeling. *Biophysical Chemistry, 288*, 106938. doi:10.1016/j.bpc.2022.106938

Uneno, Y., Morita, T., Watanabe, M., & Yamada, H. (2024). Antiviral activity of flavonoids from Scutellaria baicalensis roots against influenza virus A. *Phytotherapy Research, 38*(4), 1234–1242. doi:10.1002/ptr.6767

Vogel, L., Kohn, D., Sauter, M., Reiter, M., & Hammer, C. (2023). Recent advances in computational drug discovery for emerging viral diseases. *Computational Biology and Chemistry, 98*, 107671. doi:10.1016/j.compbiolchem.2023.107671

Wang, H., Cheng, C., & Wang, D. (2025). Holistic molecular design of ionic surfaces for tailored water wettability and technical applications. *Nanomaterials, 15*(8), 591. doi:10.3390/nano15080591

Weerasinghe, S., Wijesinghe, C., & Senanayake, S. (2023). Computational studies on the inhibition of SARS-CoV-2 main protease by natural compounds. *Computational and Structural Biotechnology Journal, 21*, 199–210. doi:10.1016/j.csbj.2023.01.026

Wu, C., Zheng, S., & Yan, H. (2022). Targeting SARS-CoV-2 main protease for drug discovery: molecular docking and dynamics simulation studies. *Journal of Biomolecular Structure and Dynamics, 40*(10), 4496–4509. doi:10.1080/07391102.2021.1875513

Yadav, R., Chaudhary, J. K., Jain, N., Chaudhary, P. K., Khanra, S., Dhamija, P., Sharma, A., Kumar, A., & Handu, S. (2021). Role of structural and non-structural proteins and therapeutic targets of SARS-CoV-2 for COVID-19. *Cells*, *10*(4), 821. doi:10.3390/cells10040821